ChemPubSoc Europe

DOI: 10.1002/cctc.201402895

CHEMCATCHEM Full Papers

Cu-Decorated Ru Catalysts Supported on Layered Double Hydroxides for Selective Benzene Hydrogenation to Cyclohexene

Jie Liu, Simin Xu, Weihan Bing, Fei Wang, Changming Li, Min Wei,* David G. Evans, and Xue Duan[a]

The selective hydrogenation of benzene to cyclohexene is of high value for the chemical industry owing to its inexpensive feedstock, atom economy, and operational simplicity. A tunable catalytic behavior towards the selective hydrogenation of benzene was obtained over Cu-decorated Ru catalysts supported on a layered double hydroxide (denoted as Ru_xCu_y/MgAl-LDH), reaching a maximum cyclohexene yield of 44.0% over $Ru_{1.0}Cu_{0.5}$/MgAl-LDH at 150 °C and 5.0 MPa without employment of any additives. CO-TPD (TPD = temperature-programmed desorption) and in situ CO-FTIR techniques demonstrated that Cu atoms preferentially deposit on the surface of low-coordinated Ru atoms in Ru_xCu_y/MgAl-LDH catalysts, resulting in a low adsorption energy of cyclohexene on the modified sites as revealed by DFT calculations. This work not only gives an understanding of the correlation between the surface exposure of Ru active sites and the resulting selectivity, but also provides a green and additive-free catalytic process for the selective hydrogenation of benzene.

Introduction

Cyclohexene is one of the most important commodity petrochemicals, and is a raw material for the production of value-added adipic acid, nylons, caprolactam, and other fine chemicals.[1] Recently, growing interest has been focused on the generation of cyclohexene by selective hydrogenation of benzene owing to the advantages over traditional production routes (e.g., dehydration of cyclohexanol, dehydrogenation of cyclohexane, and Birch reduction), in terms of inexpensive feedstock, atomic economy, and operational simplicity.[2] However, obtaining high yields of cyclohexene from the selective hydrogenation of benzene is challenging because of further hydrogenation from cyclohexene to cyclohexane.[3] Ruthenium-based catalysts are commonly used in this reaction and generally exhibit a relatively high yield of cyclohexene with the assistance of large amounts of additives (typically, $ZnSO_4$).[4–12] Although the cyclohexene yield can be increased effectively, the use of zinc salts results in corrosion and separation problems, which limit the long-term development of such a system. Therefore, the exploration of highly efficient, economical, and green catalysts for this reaction remains a challenging goal.

Given the well-known characteristics of the consecutive hydrogenation of benzene, the knowledge of how to facilitate the desorption of cyclohexene from the catalyst surface, as well as to inhibit its readsorption remains the key issue that needs to be addressed to obtain a high yield of cyclohexene.[4,9,12–14] Fundamental studies have been conducted based on the employment of hydrophilic Ru-based catalysts in an aqueous-phase-assisted catalytic system, resulting in the kinetically enhanced desorption of cyclohexene.[1a,15,16] In addition, the structure of active sites and reaction conditions (e.g., temperature, pressure, and medium) also play important roles in the adsorption behavior of cyclohexene on the catalyst surface.[4,17,18] The reported tailoring, by additives, of Ru-based catalysts with a favorable electronic and geometric structure provides important approaches for the enhancement of selectivity towards cyclohexene.[6,13,19,20] However, very few investigations were performed to reveal the influences of surface defects on the hydrogenation selectivity on an atomic basis. This investigation would be particularly interesting because metal catalysts with controlled exposure of active sites have been proven to exhibit excellent catalytic behavior in the field of hydrogenation reactions.[21,22]

One of the most promising approaches to tune metal catalysts with controlled exposure of active sites is surface modification by a second metal.[23,24] However, it is rather difficult to incorporate a suitable second metal and a facile synthesis strategy to obtain a core-shell structure similar to bimetallic particles, in which the main metal particles exhibit a controlled atom exposure owing to the surface coverage or segregation of the second metal. Layered double hydroxides (LDHs), with the formula of $[M^{2+}_{1-x}M^{3+}_x(OH)_2](A^{n-})_{x/n}\cdot mH_2O$, have been extensively explored as sorbents and heterogeneous catalysts and/or precursors because of their versatility in composition, morphology, and architecture.[25–29] Considerable interest has been focused on the design and preparation of mono-/bimetallic nanocatalysts owing to the unique topotactic transformation

[a] J. Liu, S. Xu, W. Bing, F. Wang, Dr. C. Li, Prof. M. Wei, Prof. D. G. Evans, Prof. X. Duan
State Key Laboratory of Chemical Resource Engineering
Beijing University of Chemical Technology (P.R. China)
Fax: (+86) 10-64425385
E-mail: weimin@mail.buct.edu.cn

Supporting Information for this article is available on the WWW under http://dx.doi.org/10.1002/cctc.201402895.

of LDH materials into supported metal nanocatalysts on a metal oxide matrix under reducing conditions.[30–34] Inspired by the unique merits of LDH materials, we explored the idea that bimetallic catalysts can be fabricated by a co-reduction approach. Treatment of $RuCl_3$-impregnated CuMgAl-LDH by hydrogen resulted in the formation of a supported bimetallic Ru–Cu catalyst on a $MgO–Al_2O_3$ mixed metal oxide (denoted as MgAl-MMO) matrix. This strategy possesses the following desirable features: 1) The atomic-scale distribution of Cu in the LDH precursors favors uniform decoration of Ru nanoparticles (NPs) so as to achieve a tunable catalytic performance; and 2) the co-reduction process based on the topotactic transformation of LDH guarantees the high stability of the resulting supported Ru_xCu_y NPs.

Herein, we report the fabrication of Cu-decorated Ru catalysts supported on MgAl-LDH by a facile two-step procedure involving the reduction of $RuCl_3$-impregnated CuMgAl-LDH by hydrogen, followed by the rehydration of the resulting Ru_xCu_y/MgAl-MMO to Ru_xCu_y/MgAl-LDH (Scheme 1). SEM and TEM

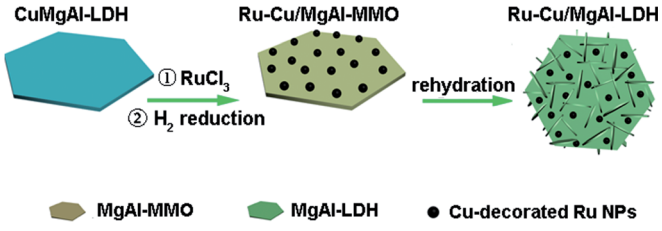

Scheme 1. The synthesis of Cu-decorated Ru nanoparticles supported on MgAl-LDH.

measurements reveal that Cu-decorated Ru particles with a mean size of ≈2.1 nm were well-dispersed on the hierarchical LDH matrix. CO-TPD (TPD = temperature-programmed desorption) and CO-FTIR measurements demonstrated that the metallic Cu tends to deposit on the surface of Ru particles at the low-coordinated sites. The resulting Ru_xCu_y/MgAl-LDH catalysts exhibit a tunable catalytic performance toward the selective hydrogenation of benzene, and the best catalytic behavior was obtained over $Ru_{1.0}Cu_{0.5}$/MgAl-LDH with a maximum cyclohexene yield of 44.0% (150 °C, 5.0 MPa). A correlation between the exposure of Ru active sites and the selectivity was established based on kinetic investigations and DFT calculations. The low-coordinated Ru atoms possess a high surface free energy, which is unfavorable for the desorption of cyclohexene; an appropriate coverage of the low-coordinated Ru by Cu gives rise to a largely enhanced selectivity toward cyclohexene. This work provides an understanding of the discriminatory hydrogenation behavior of Ru active sites, and demonstrates a promising approach for the fabrication of green catalysts for structure-sensitive hydrogenation reactions.

Results and Discussion

Structural and morphological characteristics

The CuMgAl-LDH precursors with various Cu contents were prepared by the urea hydrolysis–precipitation method.[35] The powdered XRD patterns of these precursors are shown in Figure S1 A (see the Supporting Information), in which the typical (003) and (006) reflections at $2\theta \approx 12$ and 24° are observed, respectively, verifying the formation of hydrotalcite phase. No other crystalline phase was detected, indicating the high purity of these LDH precursors. After impregnation of $RuCl_3$, followed by subsequent reduction process, two peaks at $2\theta \approx 43$ and 63° were observed (Figure S1 B), which can be indexed to the typical (200) and (220) reflections of a face-centered MgO phase. This finding confirms the topotactic transformation of the LDH precursors to mixed metal oxides accompanied by the co-reduction of Ru and Cu (Ru_xCu_y/MgAl-MMO). However, no reflections corresponding to metallic Ru and Cu were detected, possibly because of a high dispersion with tiny particle size or low concentration of metal species in these samples, which was outside of the XRD detection limit.

Taking into account the fact that the selective hydrogenation of benzene is actually performed in an aqueous microenvironment system,[1a,15,16] the choice of a good hydrophilic support for the immobilization of the metal catalyst is important. Herein, the Ru_xCu_y/MgAl-MMO samples underwent further treatment by a rehydration process, so as to achieve the transformation of the catalyst support from MMO to LDH based on the so-called "memory effect" of LDH materials.[36] It was found that the typical (003) and (006) reflections for the hydrotalcite phase reappear in the XRD patterns of the regenerated samples (Figure 1), indicative of successful fabrication of Ru_xCu_y/MgAl-LDH samples from Ru_xCu_y/MgAl-MMO. Compared with the original CuMgAl-LDH precursors (Figure S1 A), the full width at half maximum (FWHM) of the regenerated Ru_xCu_y/MgAl-LDH is much wider, suggesting a decrease in the crystalline degree of the LDH phase. FTIR spectra show a strong peak at 3470 cm^{-1}, attributed to the stretching mode of surface hydroxyl groups (Figure S2),[37] which implies good hydrophilicity for these LDH materials. The peaks at 1360 and 3070 cm^{-1} are assigned to the stretching vibration of interlayer CO_3^{2-} and the bridging mode of $H_2O–CO_3^{2-}$, respectively, which confirms the formation of carbonate-containing LDH materials.

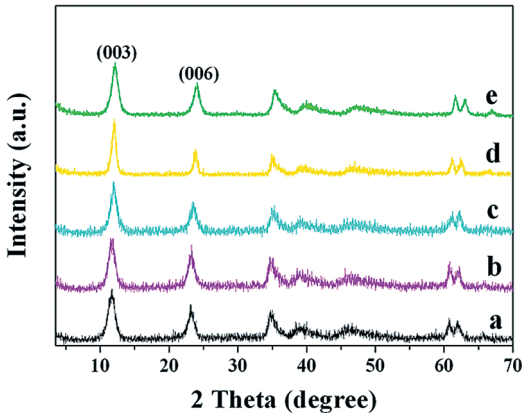

Figure 1. XRD patterns of a) Ru/MgAl-LDH, b) $Ru_{1.0}Cu_{0.2}$/MgAl-LDH, c) $Ru_{1.0}Cu_{0.5}$/MgAl-LDH, d) $Ru_{1.0}Cu_{1.0}$/MgAl-LDH, and e) Cu/MgAl-LDH-2 derived from CuMgAl-LDH-2 precursor.

The SEM images of three typical samples: CuMgAl-LDH-2 precursor, $Ru_{1.0}Cu_{0.5}$/MgAl-MMO, and $Ru_{1.0}Cu_{0.5}$/MgAl-LDH are shown in Figure 2. The LDH precursor displays smooth and uniform hexagonal nanocrystals with a diameter of ≈2 μm (Figure 2a and b). Hydrogen reduction of the $RuCl_3$-impregnated CuMgAl-LDH-2 resulted in its transformation to $Ru_{1.0}Cu_{0.5}$/MgAl-MMO, which still maintains the original morphology of the LDH precursor (Figure 2c). After the further rehydration treatment of $Ru_{1.0}Cu_{0.5}$/MgAl-MMO, an interesting morphological change occurs. A large number of nanosheets are observed on the surface of an individual hexagonal nanocrystal (Figure 2d). A similar phenomenon was also observed for other Ru_xCu_y/MgAl-LDH samples (Figure S3). This structural transformation from Ru_xCu_y/MgAl-MMO to Ru_xCu_y/MgAl-LDH is due to the so-called "memory effect" of calcined hydrotalcite, that is, it can recover the original LDH structure with a positively charged host layer and an interlayer CO_3^{2-} as a compensation anion.[36]

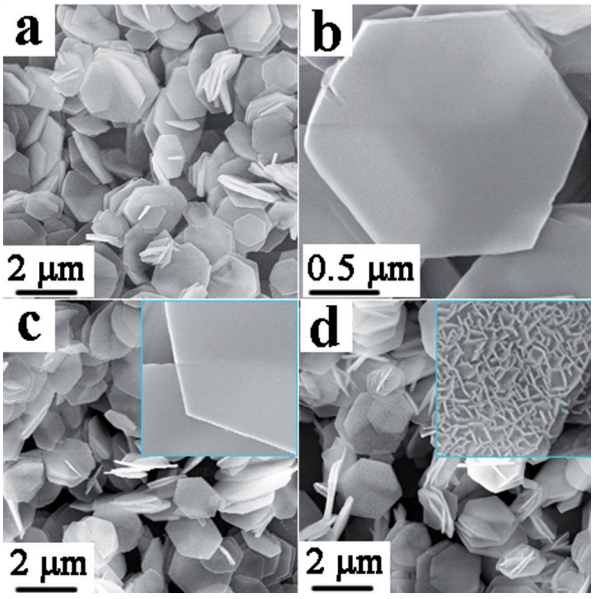

Figure 2. SEM images of a, b) CuMgAl-LDH-2 precursor, c) $Ru_{1.0}Cu_{0.5}$/MgAl-MMO, and d) regenerated $Ru_{1.0}Cu_{0.5}$/MgAl-LDH.

HRTEM measurements were employed to investigate the structure and distribution of metal species (i.e., Ru and Cu) on MgAl-MMO and the regenerated MgAl-LDH. For the Ru_xCu_y/MgAl-MMO samples, metal nanoparticles with high density disperse uniformly in a platelet-like matrix, as shown in Figure 3 a_1–d_1. The histograms (Figure 3 a_1–d_1, inset) show that all four samples possess a narrow size distribution from 1.5 to 2.7 nm, with a mean size of 2.1 nm based on 300 particles counted in different regions. The corresponding HRTEM images with high magnification (Figure 3 a_2–d_2) reveal nanoparticles with characteristic lattice spacing of 0.206 nm, which can be ascribed to the (1 0 1) plane of hexagonal close-packed (hcp) Ru. This finding is further confirmed by the fast Fourier transform (FFT) patterns (Figure 3 a_2–d_2, inset). A metallic Cu phase is not observed for the four samples, suggesting that Cu is deposited onto the surface of Ru particles because the two metals are immiscible in bulk. To study the evolution of Cu, we increased the Cu content gradually, and found an individual metallic Cu atom cannot be identified until the Cu/Ru molar ratio increases to 3:1 (Figure S5). Similar phenomena were also reported for Ru–Cu bimetal NPs supported on other carriers (e.g., KL-zeolite and SiO_2),[38,39] in which the tiny metallic Cu atoms deposit on the surface of Ru at a low concentration, and tend to form segregated Cu particles at a high concentration. The XPS spectra of Ru 3d and Cu 2p (Figure S6) reveal the presence of metallic Ru and Cu in the Ru_xCu_y/MgAl-MMO samples. The peak at 280.2 eV can be attributed to the binding energy of Ru $3d_{5/2}$ (Figure S6A);[40] whereas the two peaks at 952. 5 and 932.8 eV can be attributed to Cu $2p_{3/2}$ and Cu $2p_{1/2}$, respectively (Figure S6B).[41] Both of the binding energies of Ru and Cu do not show any shift for these samples with various Ru/Cu ratios, indicating the absence of obvious electron interaction. Regard-

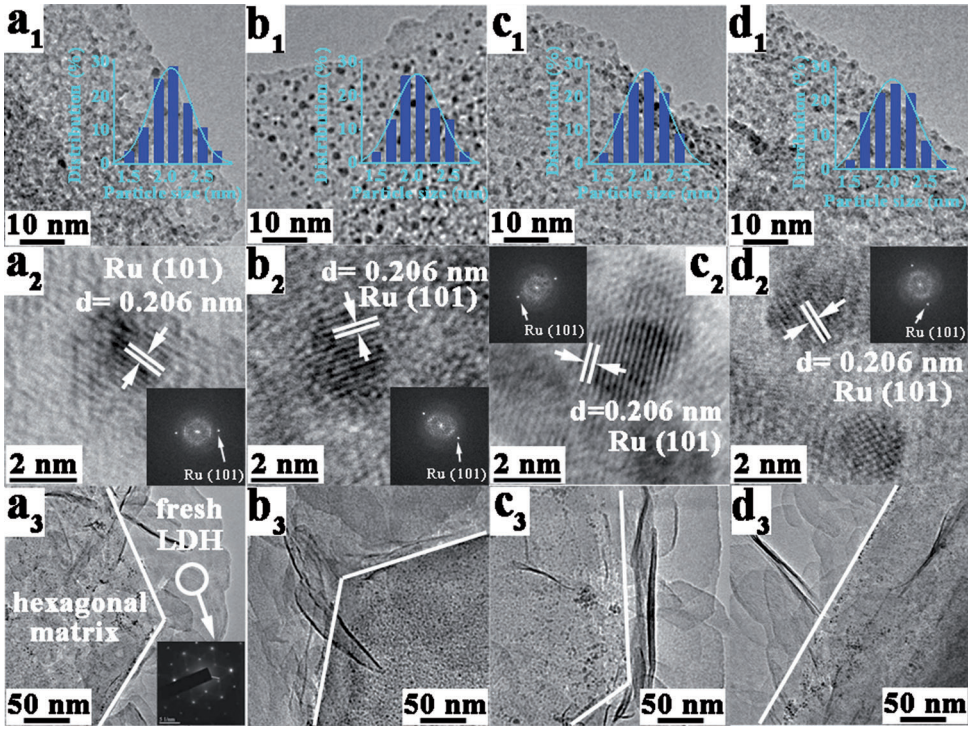

Figure 3. HRTEM images of the Ru_xCu_y/MgAl-MMO and the corresponding Ru_xCu_y/MgAl-LDH samples: a_1, a_2) Ru/MgAl-MMO, b_1, b_2) $Ru_{1.0}Cu_{0.2}$/MgAl-MMO, c_1, c_2) $Ru_{1.0}Cu_{0.5}$/MgAl-MMO, d_1, d_2) $Ru_{1.0}Cu_{1.0}$/MgAl-MMO, a_3) Ru/MgAl-LDH, b_3) $Ru_{1.0}Cu_{0.2}$/MgAl-LDH, c_3) $Ru_{1.0}Cu_{0.5}$/MgAl-LDH, d_3) $Ru_{1.0}Cu_{1.0}$/MgAl-LDH. Insets in (a_1), (b_1), (c_1), and (d_1) are the corresponding particle-size frequency distribution histograms (300 particles analyzed).

ing the low intensity of the XPS spectra of Cu, Cu K-edge X-ray-absorption near-edge structure (XANES) spectra are also given in Figure S7. It was found that the Cu K-edge XANES of the three Cu-containing samples was rather close to that of Cu foil, further verifying the presence of metallic Cu in these Ru–Cu samples. Figure 3 a_3–d_3 further shows that the metal NPs were still well-dispersed on the basal hexagonal matrix after the regeneration process, with epitaxially-formed LDH nanosheets. The inset in Figure 3 a_3 shows a hexagonal arrangement of spots from the fresh LDH nanosheets in the corresponding selected-area electron diffraction (SAED) pattern. This arrangement demonstrates a well-crystallized hydrotalcite phase[42] owing to the epitaxial growth of nanosheets. This finding is in accordance with the XRD results (Figure 1). Moreover, HRTEM images of the Ru_xCu_y/MgAl-LDH samples with high magnification (Figure S8) further shows that the morphology of the bimetal NPs remains unchanged after the rehydration process.

Hydrogen temperature-programmed reduction (H_2-TPR) measurements were performed to provide information on the redox properties of $RuCl_3$-impregnated CuMgAl-LDH samples (Figure 4 A). Two peaks at around 125 and 270 °C can be observed in the H_2-TPR profiles of these samples. The first peak is attributed to the reduction of Ru species,[43] whereas the second peak is attributed to the reduction of Cu^{2+} species in the lamellar structure,[44] verifying the strong reducibility of Ru species, which undergoes preferential reduction. It can be seen that the hydrogen consumption for the reduction of Cu^{2+} species increases gradually along with the increase of Cu content (Figure 4 A, a–d), whereas no obvious change was observed for the reduction peak of Ru. Therefore, it is deduced that the preferentially reduced Ru particles may act as the seeds for the subsequent reduction of Cu oxide, resulting in the Cu-decorated Ru particles in the above samples. Carbon monoxide temperature-programmed desorption (CO-TPD) experiments were further employed to investigate the influence of Cu on the surface-atom exposure of metallic Ru particles in the final Ru_xCu_y/MgAl-LDH samples (Figure 4 B). A strong desorption peak of CO at 170 °C can be observed in the CO-TPD profiles of the four Ru-based samples (Figure 4 B, a–d), whereas no obvious CO chemisorption can be found for the Cu/MgAl-LDH-2 sample derived from the CuMgAl-LDH-2 precursor (Figure 4 B, e). This result indicates that for the Ru–Cu bimetallic system, CO chemisorption occurs on Ru, but not on Cu, at room temperature.[38] In addition, for the four Ru-based samples, the intensity of the desorption peak of CO decreases gradually with the increase of Cu content, indicating a decreased chemisorption capacity of CO in the Ru_xCu_y/MgAl-LDH samples. Based on the CO chemisorption capacity, the apparent dispersion of Ru in these Ru-based samples was calculated and is listed in Table 1. Because the four samples possess a similar Ru particle size (Figure 3), the apparent decline of Ru dispersion upon increasing Cu content further confirms the deposition of Cu atoms on the surface of the Ru particle.

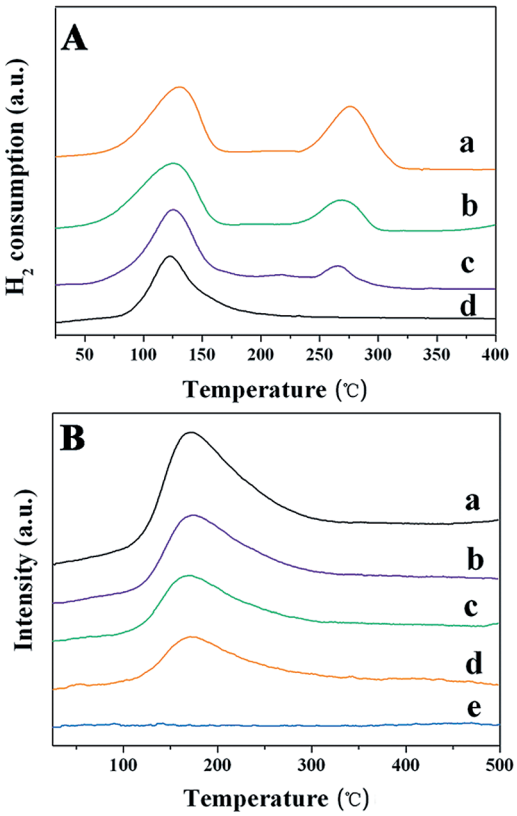

Figure 4. A) H_2-TPR profiles of: a) Ru/CuMgAl-LDH-0, b) Ru/CuMgAl-LDH-1, c) Ru/CuMgAl-LDH-2, and d) Ru/CuMgAl-LDH-3. B) CO-TPD profiles of: a) Ru/MgAl-LDH, b) $Ru_{1.0}Cu_{0.2}$/MgAl-LDH, c) $Ru_{1.0}Cu_{0.5}$/MgAl-LDH, d) $Ru_{1.0}Cu_{1.0}$/MgAl-LDH, and e) Cu/MgAl-LDH-2.

In heterogeneous catalysis, metal particles involve various active sites (e.g., corners, steps, and facets). The deposition of Cu on the surface of Ru particles leads to a decreased exposure of Ru active sites, but detailed information on the preferentially covered active sites is still not available. In situ FTIR spectra of CO adsorption is a useful method to probe the surface structure of Ru particles. The IR spectra of CO absorbed on the five Ru_xCu_y/MgAl-LDH samples are shown in Figure 5. For the Cu/MgAl-LDH sample, no obvious CO vibration was ob-

Table 1. Structural parameters of various samples.

Catalyst	S_{BET} [$m^2 g^{-1}$]	Ru [wt.%][a]	Molar ratio of Ru/Cu[a]	Apparent dispersion of Ru [%][b]	Coverage degree (θ) of Cu [%][b]	Mean particle size by TEM [nm]
Ru/MgAl-LDH	38	2.39 ± 0.05	1:0	26.5	0	2.1 ± 0.6
$Ru_{1.0}Cu_{0.2}$/MgAl-LDH	38	2.48 ± 0.05	1:0.18	21.1	17.2	2.0 ± 0.6
$Ru_{1.0}Cu_{0.5}$/MgAl-LDH	40	2.51 ± 0.07	1:0.45	17.9	29.1	2.0 ± 0.6
$Ru_{1.0}Cu_{1.0}$/MgAl-LDH	40	2.45 ± 0.04	1:0.82	13.8	46.6	2.1 ± 0.6

[a] Values determined by ICP. [b] Values calculated based on CO-TPD.

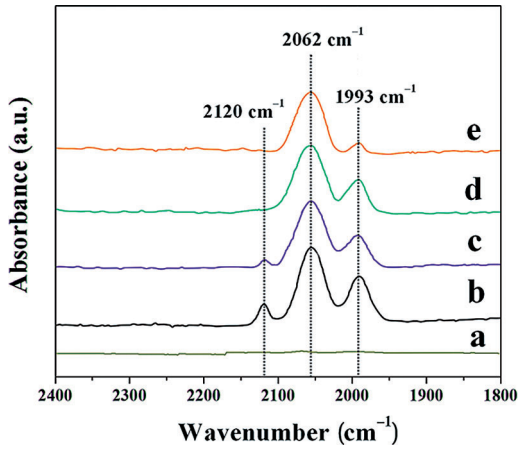

Figure 5. In situ FTIR spectra of CO adsorption on a) Cu/MgAl-LDH-2, b) Ru/MgAl-LDH, c) $Ru_{1.0}Cu_{0.2}$/MgAl-LDH, d) $Ru_{1.0}Cu_{0.5}$/MgAl-LDH, and e) $Ru_{1.0}Cu_{1.0}$/MgAl-LDH.

served (Figure 5a), in accordance with the CO-TPD result (Figure 4e), further confirming that Cu^0 hardly adsorbs CO species at room temperature.[38] In the case of the Ru/MgAl-LDH sample, three bands can be identified (Figure 5b). The bands at 1993 and 2062 cm^{-1} can be attributed to the bridge-bonded and linearly adsorbed CO on Ru atoms, respectively; whereas the band at 2120 cm^{-1} can be assigned to the stretching mode of multicarbonyl species, which often adsorb on low-coordinated sites (such as corners, steps, or defective sites) of finely dispersed noble metals.[23,45] Generally, low-coordinated metal atoms possess relatively low electron density and lead to the occurrence of the stretching vibration of multicarbonyls at a high wavenumber, owing to the weak electron feedback to the adsorbed CO. Of the four Ru-based samples, Ru/MgAl-LDH exhibits the strongest multi-CO adsorption (Figure 5b), indicating a high exposure of unsaturated Ru. With the introduction of Cu, the adsorption intensity of multi-CO decreases gradually and reaches a negligible value at a Ru/Cu molar ratio of 1:0.5 and 1:1 (Figure 5d and e), implying almost complete coverage of Cu on the low-coordinated Ru. The coverage degree of Cu (θ_{Cu}) for these two samples is ≈29.1 and 46.6%, respectively, according to the CO-TPD result (Table 1). The results indicate a preferential coverage of Cu on the low-coordinated Ru, in good agreement with previous investigations.[46] For the bridge-bonded CO adsorption peak at 1993 cm^{-1}, a continuous decrease is observed with the enhancement of Cu content to the Cu/Ru molar ratio of 1:1 (Figure 5e), implying a further coverage of Cu on the high-coordinated Ru. Therefore, a tunable exposure of the active sites of Ru NPs can be successfully achieved by changing the surface coverage of Cu originating from a LDH support. This finding imposes great influence on the hydrogenation selectivity, which is discussed below.

Catalytic evaluation for selective hydrogenation of benzene

The catalytic performances of the as-synthesized Ru/MgAl-LDH and Ru_xCu_y/MgAl-LDH samples were evaluated by the selective hydrogenation of benzene to cyclohexene. The corresponding plots of the selectivity for cyclohexene versus the conversion of benzene are shown in Figure 6 (reaction temperature: 150 °C; H_2 pressure: 5.0 MPa). The benzene content decreased gradually and the completely saturated product, cyclohexane, increased linearly with reaction time. Regarding the cyclohexene content, there was a maximum at a certain reaction time, dependent on the catalyst, exhibiting the well-known behavior of consecutive reactions. Among the four catalysts, the Ru/MgAl-LDH catalyst shows the highest activity of benzene hydrogenation, but the lowest selectivity to cyclohexene. With the enhancement of incorporated Cu, the activity of benzene hydrogenation over the resulting Ru_xCu_y/MgAl-LDH decreased gradually, whereas the selectivity to cyclohexene increased and reached a maximum value at a Ru/Cu molar ratio of 1:0.5. As a result, a maximum cyclohexene yield of 44.0% at a benzene conversion of 71.8% was obtained over the $Ru_{1.0}Cu_{0.5}$/MgAl-LDH catalyst. Although the obtained catalytic yield is not as high as some reported values, the Cu-decorated Ru catalyst in this work does not involve the use of any additive (e.g., $ZnSO_4$), which has been commonly applied previously (see Table S1). Therefore, this additive-free catalyst can serve as a green and eco-friendly candidate for the selective hydrogenation of benzene.

It can be seen from Figure 6 that all three Ru_xCu_y/MgAl-LDH catalysts display inhibited activity of benzene hydrogenation with the addition of Cu, in comparison with the Ru/MgAl-LDH catalyst. As summarized in Table 2, the weight-specific activity (R_0) of these catalysts also decreased with an increase of Cu content. This inhibiting effect, to some extent, can be attributed to the coverage of Cu on the surface of Ru, resulting in a decreased exposure of Ru active sites. To give a deep insight into the inhibition effect, the turnover frequency (TOF) of benzene over these catalysts was further calculated on the basis of Ru dispersion and R_0 data. A plot of the TOF value as a function of the coverage degree of Cu (θ_{Cu}) is shown in Figure 7a. It is observed that initially the TOF value exhibits a linear decrease with an increase of θ_{Cu}, and is balanced at a θ_{Cu} value of 29.1%. It has been proven that metal catalysts with high unsaturation/low coordination number generally show excellent hydrogenation activity.[47] For benzene hydrogenation, a high efficiency of hydrogenation is also dependent on the exposure of low-coordinated Ru atoms.[20] Compared with the Ru/MgAl-LDH catalyst, the low-coordinated Ru atoms in the Ru_xCu_y/MgAl-LDH catalysts are continuously covered by Cu and undergo a complete coverage at θ_{Cu} value of 29.1%, according to the CO-TPD result, which accounts for the gradually decrease in the TOF of benzene.

Although the reaction rate of benzene hydrogenation over the Cu-decorated Ru catalysts was inhibited to some extent, the hydrogenation selectivity to cyclohexene was largely enhanced. In terms of the effect of Cu on the cyclohexene selectivity for these catalysts, the value of $S_{50,CHE}$ was also obtained (defined as the cyclohexene selectivity at 50% benzene conversion). Unlike the negative correlation between the TOF value and the coverage of Cu on the Ru surface, a positive relationship was established for $S_{50,CHE}$ (Figure 7b), indicative of

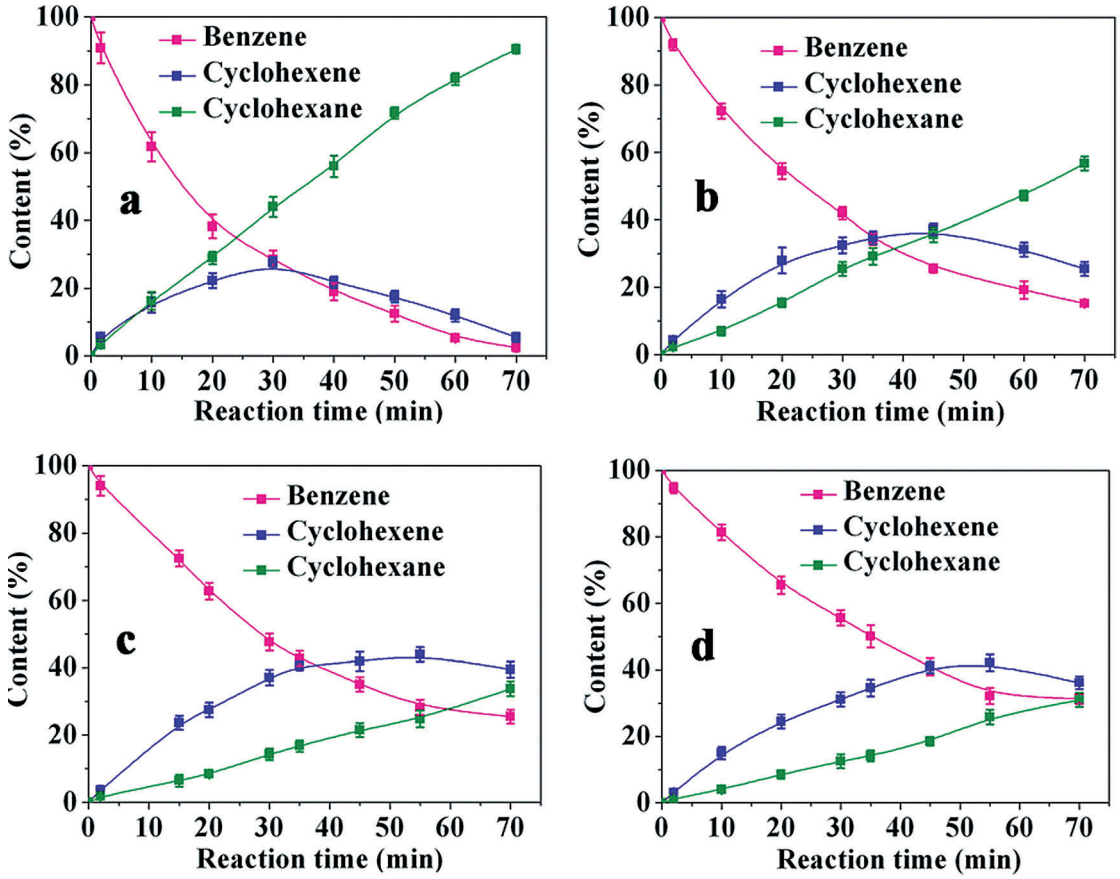

Figure 6. The time courses of benzene hydrogenation over a) Ru/MgAl-LDH, and the Ru_xCu_y/MgAl-LDH catalysts with various Ru/Cu ratios: b) 1:0.2, c) 1:0.5, d) 1:1. Reaction conditions: catalyst (0.1 g), benzene (10 mL), H_2O (20 mL), temperature (150 °C), H_2 pressure (5.0 MPa), stirring rate (1000 rpm).

Table 2. Catalytic performance of various catalysts.[a]

Catalyst	t [min][b]	Conv. [%][b]	S_{CHE} [%][b]	Y_{CHE} [%][b]	$S_{50,CHE}$ [%]	$STY_{50,CHE}$ [mmol min^{-1} g^{-1}_{Ru}]	R_0 [mmol min^{-1} g^{-1}][c]	TOF [s^{-1}]
Ru/MgAl-LDH	30.0	71.5 ± 2.6	38.6 ± 3.8	27.5 ± 1.7	35.4 ± 2.7	488 ± 18	67.7 ± 1.5	18.0 ± 0.4
$Ru_{1.0}Cu_{0.2}$/MgAl-LDH	45.0	74.4 ± 1.2	50.1 ± 2.2	37.2 ± 1.7	60.6 ± 3.1	597 ± 11	43.2 ± 1.9	13.9 ± 0.3
$Ru_{1.0}Cu_{0.5}$/MgAl-LDH	55.0	71.8 ± 2.2	61.3 ± 2.6	44.0 ± 2.1	70.8 ± 2.4	566 ± 12	29.1 ± 1.1	10.9 ± 0.4
$Ru_{1.0}Cu_{1.0}$/MgAl-LDH	55.0	68.9 ± 2.5	61.2 ± 3.6	42.1 ± 2.5	69.8 ± 2.8	467 ± 10	21.7 ± 1.3	10.8 ± 0.3

[a] Reaction conditions: Catalyst (0.1 g), benzene (10 mL), H_2O (20 mL), H_2 pressure (5.0 MPa), 150 °C. [b] The results are provided at the maximum yield of cyclohexene. Conv. = conversion of benzene; S_{CHE} = selectivity to cyclohexene; Y_{CHE} = yield of cyclohexene; $S_{50,CHE}$ refers to the selectivity to cyclohexene at which a benzene conversion of 50% is obtained. $STY_{50,CHE}$ refers to the space-time-yield to cyclohexene and was calculated based on the amount of cyclohexene produced per minute per gram of metal Ru at a benzene conversion of 50%. [c] Values were calculated based on the amount of converted benzene per minute per gram of catalyst.

the TPD result, which accounts for the gradually decrease in the TOF of benzene. Because the selectivity to cyclohexene is determined by the relative hydrogenation rate of benzene to cyclohexene (step 1) and of cyclohexene to cyclohexane (step 2), further understanding of the reaction kinetics is necessary. By fitting the reaction data presented in Figure 6, a first-order reaction for step 1 and a zero-order reaction for step 2 were identified, and are consistent with previous reports.[48] The relative kinetic plots are shown in Figure 8, from which the rate constants k_1 and k_2 for the two hydrogenation steps were calculated and are listed in Table 3. The results show that both step 1 and step 2 are slowed by the coverage of Cu on the Ru surface (Table 3); however, the decrease in the k_1 and k_2 values is not to the same extent. As listed in Table 3, the evolution of the k_1/k_2 ratio almost mimics that of $S_{50,CHE}$, implying that the coverage of Cu on the low-coordinated Ru improves the selectivity to cyclohexene by modifying the hydrogenation rates of both benzene and cyclohexene. As a result, both enhanced selectivity and space-time-yield ($STY_{50,CHE}$) can be obtained over the Cu-decorated Ru catalysts.

Generally, Cu is considered to be inactive in the catalytic hydrogenation of benzene. The "hydrogen-spillover effect" between Ru and Cu,[49] to some extent favors the hydrogenation ability of Cu.[50] However, in the case of the selective hydroge-

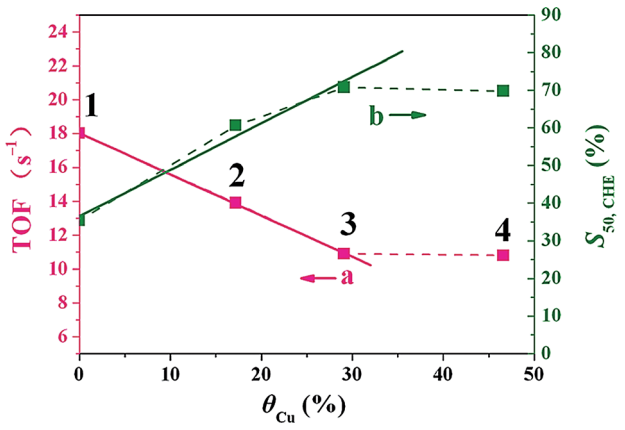

Figure 7. a) TOF and b) $S_{50,CHE}$ value as a function of the surface coverage of Ru over: 1) Ru/MgAl-LDH, 2) $Ru_{1.0}Cu_{0.2}$/MgAl-LDH, 3) $Ru_{1.0}Cu_{0.5}$/MgAl-LDH, and 4) $Ru_{1.0}Cu_{1.0}$/MgAl-LDH catalyst.

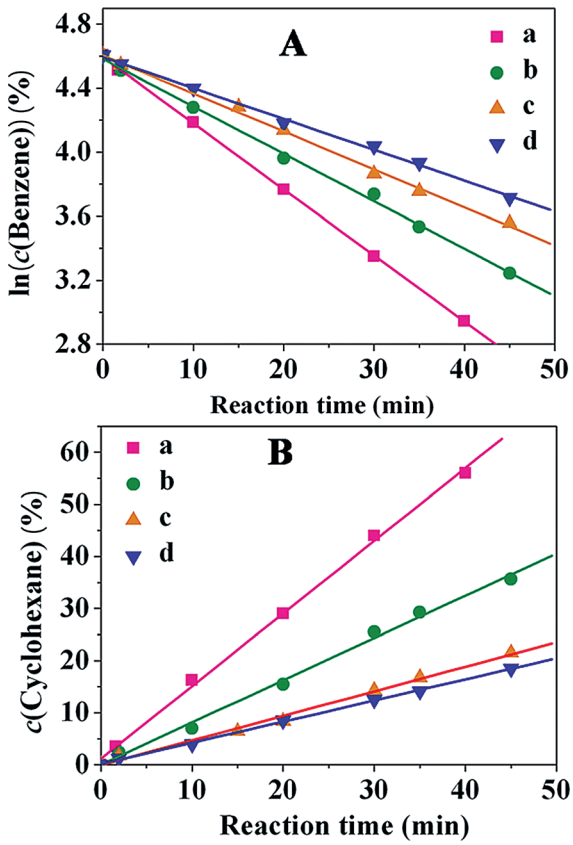

Figure 8. A) Curves of ln(*c*(benzene)) versus reaction time, B) curves of *c*(cyclohexane) versus reaction time at 150 °C and 5.0 MPa of hydrogen: a) Ru/MgAl-LDH, b) $Ru_{1.0}Cu_{0.2}$/MgAl-LDH, c) $Ru_{1.0}Cu_{0.5}$/MgAl-LDH, and d) $Ru_{1.0}Cu_{1.0}$/MgAl-LDH.

nation of benzene to cyclohexene, the enhanced hydrogenation capability of Cu could facilitate further hydrogenation of cyclohexene to cyclohexane, which is unfavorable to improve the reaction selectivity.[6] It is well-known that the low-coordinated atoms are generally associated with defects, edges, corners, or high-index facets, which normally exhibit a high surface-adsorption energy. The presence of the high-energy adsorption sites does not favor desorption of the formed cyclohexene and thus reduces the hydrogenation selectivity. To provide further evidence, DFT calculations were performed to investigate the adsorption energy of cyclohexene on the surface of Ru with different coordination numbers. As depicted in Figure S9, the adsorption energy of cyclohexene on high-coordinated metallic Ru(0 0 0 1) facet is lower than that on the low-coordinated Ru(1 1 2 2) facet (E_{ads} on Ru(0 0 0 1) and Ru (1 1 2 2): 4.30 and 4.62 eV, respectively). As far as the Ru_xCu_y/MgAl-LDH catalytic system is concerned, the occupancy of Cu on the low-coordinated Ru can be regarded as a restrained exposure of a high-index facet of Ru. Thus, desorption of cyclohexene on the Cu-decorated Ru particles becomes easy, and its further hydrogenation to cyclohexane is prevented. Furthermore, the adsorption energy of cyclohexene on the typical Ru(0 0 0 1) facet with the modification of Cu cluster was calculated, from which a decreased E_{ads} (3.78 eV) was obtained (Figure S9c). Therefore, in view of the decreased hydrogenation activity with the addition of Cu, as well as the low adsorption energy of cyclohexene on Cu-decorated Ru catalyst, it is concluded that the "shielding effect" of Cu gives a dominant contribution to the enhanced selectivity towards cyclohexene.

In addition, it has been reported that the hydrophilicity of the catalyst support imposes an important effect on its selectivity.[4,18] Therefore, we performed a study to investigate this effect. The catalytic behavior of Ru_xCu_y/MgAl-MMO samples with the same active center, but a less-hydrophilic support was also studied. Compared with the Ru_xCu_y/MgAl-LDH catalysts, the corresponding Ru_xCu_y/MgAl-MMO samples exhibited a much lower cyclohexene yield, with the highest value of 33.4% over $Ru_{1.0}Cu_{0.5}$/MgAl-MMO (Figure S10). This lower yield can be attributed to the relatively poor hydrophilicity of the MgAl-MMO support. For the selective hydrogenation of benzene, a good hydrophilic support makes Ru catalysts well-dispersed in the aqueous phase, which is favorable for desorption of low-soluble cyclohexene from the catalyst surface. During the rehydration process, the MgAl-MMO support converts into a hydroxyl-enriched MgAl-LDH support, which endows an excellent hydrophilicity for the resulting Ru_xCu_y/MgAl-LDH cata-

Table 3. The rate constants for the hydrogenation of benzene to cyclohexene (k_1) and cyclohexene to cyclohexane (k_2) over Ru_xCu_y/MgAl-LDH catalysts.

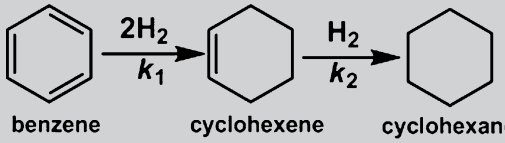

Catalyst	k_1 [10^{-2} min^{-1}][a]	k_2 [10^{-2} mol L^{-1} min^{-1}][a]	k_1/k_2 [10^{-2} L mol^{-1}]
Ru/MgAl-LDH	4.13	140	2.95
$Ru_{1.0}Cu_{0.2}$/MgAl-LDH	2.96	81.1	3.65
$Ru_{1.0}Cu_{0.5}$/MgAl-LDH	2.37	47.2	5.02
$Ru_{1.0}Cu_{1.0}$/MgAl-LDH	1.93	40.7	4.74

[a] Values obtained by fitting the reaction data in Figure 6.

lysts. As shown in the XPS spectra of O 1s (Figure S11), a largely enhanced oxygen-in-water (O_{H2O}) and surface-hydroxyl-oxygen (O_{OH}) concentration is present in the Ru/MgAl-LDH sample compared with Ru/MgAl-MMO, verifying the enhanced hydrophilicity of the LDH material. Finally, the recyclability of the optimal catalyst, $Ru_{1.0}Cu_{0.5}$/MgAl-LDH, was tested. After each catalytic run, the organic phase was removed under vacuum and the residual catalyst suspension was reused in a successive run without further catalyst reactivation. The catalyst exhibited good reusability, with a stable activity and selectivity after five recycles (Figure 9a). The TEM image of the used catalyst further reveals that the particle size and morphology was maintained (Figure 9b), demonstrating a stable, effective, and recyclable catalyst.

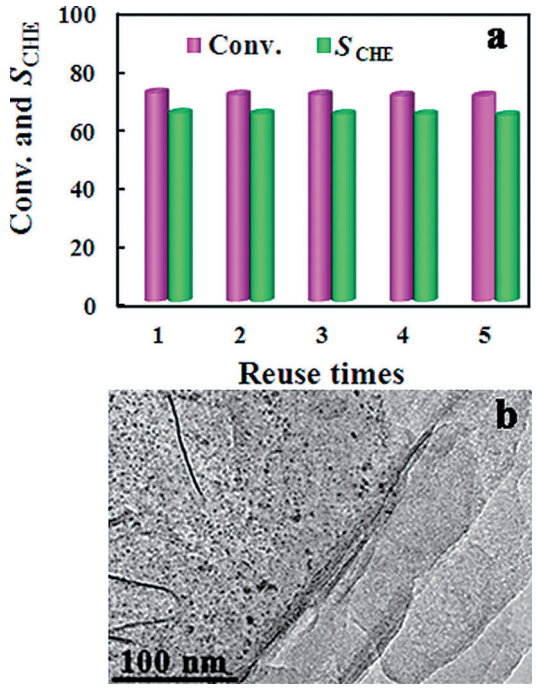

Figure 9. a) The catalytic performances of $Ru_{1.0}Cu_{0.5}$/MgAl-LDH in five consecutive recycles. b) The TEM image of $Ru_{1.0}Cu_{0.5}$/MgAl-LDH sample after five cycles.

Conclusions

In summary, the Ru_xCu_y/MgAl-LDH catalysts with a good hydrophilicity were fabricated by the co-reduction of Ru-impregnated CuMgAl-LDH, followed by LDH regeneration, and exhibit a tunable catalytic behavior towards the selective hydrogenation of benzene to cyclohexene. CO-TPD analysis demonstrates the deposition of Cu atoms on the surface of the Ru NPs, with a preferential occupancy on low-coordinated Ru as revealed by CO-FTIR analysis. The resulting Cu-decorated Ru catalysts demonstrate significantly improved catalytic selectivity for cyclohexene, and the best catalytic behavior can be obtained over the $Ru_{1.0}Cu_{0.5}$/MgAl-LDH catalyst (cyclohexene yield of 44.0% at 150 °C and 5.0 MPa) without the use of any additives. The remarkable increase in cyclohexene selectivity can be attributed to the inhibited exposure of the undesirable low-coordinated Ru species owing to the coverage of Cu, thus facilitating desorption of cyclohexene from the surface of Ru, as revealed by the DFT calculations. Understanding the "shielding effect" of the undesirable Ru active sites by an inactive ingredient could contribute to the design of more efficient catalysts. In addition, the Cu-decorated Ru catalyst does not involve the use of any corrosive additives, which have been commonly applied previously, and can serve as a green and eco-friendly candidate for the selective hydrogenation of benzene.

Experimental Section

Materials

$RuCl_3 \cdot 3H_2O$, $Cu(NO_3)_2 \cdot 3H_2O$, $Mg(NO_3)_2 \cdot 6H_2O$, and $Al(NO_3)_3 \cdot 9H_2O$ were purchased from Sigma–Aldrich. Other chemicals, including urea, benzene, cyclohexene, and cyclohexane were purchased from the Beijing chemical Co., Ltd., and used without further purification. Deionized water was used in all experimental processes.

Synthesis of CuMgAl-LDH precursors with various Cu content

CuMgAl-LDH precursors with various Cu content were synthesized by precipitation through urea hydrolysis.[35] Typically, $Mg(NO_3)_2 \cdot 6H_2O$ (10 mmol), $Al(NO_3)_3 \cdot 9H_2O$ (5 mmol), and urea (50 mmol) with various contents of $Cu(NO_3)_2 \cdot 3H_2O$ (0, 4.8×10^{-2}, 12×10^{-2}, and 24×10^{-2} mmol) were dissolved in deionized water (50 mL). The mixed solution was added into a Teflon-lined stainless steel autoclave (100 mL), sealed, and hydrothermally treated at 110 °C for 24 h. After cooling to RT, the resulting product was filtered, washed thoroughly with deionized water and ethanol, and dried in an air-circulating oven at 60 °C for 12 h. For convenience, the resulting CuMgAl-LDH samples with Cu content in ascending order are denoted as CuMgAl-LDH-0, CuMgAl-LDH-1, CuMgAl-LDH-2 and CuMgAl-LDH-3.

Synthesis of Ru_xCu_y/MgAl-MMO

Introduction of Ru was achieved through the impregnation method. The obtained CuMgAl-LDH precursors were added to a $RuCl_3 \cdot 3H_2O$ solution (40 mL, 6 mM), resulting in the Ru/Cu molar ratios 1:0, 1:0.2, 1:0.5, and 1:1. After vigorous stirring for 2 h, the precipitate was washed with deionized water until no Cl^- was detected by $AgNO_3$, and then dried in an air-circulating oven at 60 °C for 12 h, yielding Ru/CuMgAl-LDH-0, Ru/CuMgAl-LDH-1, Ru/CuMgAl-LDH-2 and Ru/CuMgAl-LDH-3. Subsequently, the obtained samples underwent a reduction process in 10% H_2 (H_2/N_2 = 1:9, v/v) at 400 °C for 3 h with a heating rate of 5 °C min^{-1}, yielding Ru–Cu bimetal NPs supported on MgO–Al_2O_3 mixed metal oxides (MgAl-MMO), which are denoted as Ru_xCu_y/MgAl-MMO with various *x*(Ru):*y*(Cu) ratios of 1:0, 1:0.2, 1:0.5 and 1:1, according to the Ru/Cu ratio in the feed.

Synthesis of Ru_xCu_y/MgAl-LDH

The Ru_xCu_y/MgAl-MMO samples underwent a rehydration process. In detail, Ru_xCu_y/MgAl-MMO (0.5 g) was added into water (50 mL) and aged in a round-bottomed flask (100 mL) at room temperature

for 1 h in CO_2 atmosphere with a flow rate of 20 mL min^{-1}. The obtained product was filtered and dried under vacuum at 50 °C for 5 h to yield the corresponding Ru/MgAl-LDH, $Ru_{1.0}Cu_{0.2}$/MgAl-LDH, $Ru_{1.0}Cu_{0.5}$/MgAl-LDH and $Ru_{1.0}Cu_{1.0}$/MgAl-LDH catalysts.

Catalytic evaluation

The selective hydrogenation of benzene was performed in a Teflon-lined stainless-steel autoclave (100 mL) equipped with a magnetic stirrer (see Figure S12). In a typical experiment, benzene (10 mL), catalyst (0.1 g), and water (20 mL) were introduced into the reactor. After being purged by low-pressure hydrogen four times to remove the air, the reactor was heated to the reaction temperature. Hydrogen was then charged into the reactor until the desired pressure was reached. The products were collected from the sample valve of the reactor and analyzed by using a gas chromatograph (GC-2014C) equipped with a flame ionization detector (FID) and a PEG-20 M capillary column (0.25 mm in diameter, 30 m in length).

Characterization

XRD patterns of samples were obtained on a Rigaku XRD-6000 diffractometer using $Cu_{K\alpha}$ radiation ($\lambda = 0.154$ nm) at 40 kV, 40 mA, a scanning rate of 10° min^{-1}, a step size of 0.02° s^{-1}, and a 2θ angle ranging from 3 to 70°. The morphology of the samples was investigated by using a Zeiss Supra 55 scanning electron microscope with an accelerating voltage of 20 kV. The actual loadings of Ru and Cu were analyzed by using a Shimadzu ICPS-7500 inductively coupled plasma emission spectrometer (ICP-ES). Prior to analysis, the sample (0.1 g) was added into 20 mL Teflon-lined stainless-steel autoclave containing concentrated nitric acid (2 mL) and concentrated hydrochloric acid (6 mL), sealed and hydrothermally treated at 150 °C for 4 h. The obtained solution was diluted with water to 100 mL. Low-temperature N_2 adsorption–desorption experiments were carried out by using the Quantachrome Autosorb-1C-VP instrument. The sample was outgassed prior to analysis at 100 °C for 12 h under 10^{-4} Pa vacuum. The total specific surface area was evaluated from the multipoint BET method. The vacuum FTIR spectra were recorded by using a Vector22 (Bruker) spectrophotometer in the range 4000–400 cm^{-1} with 2 cm^{-1} of resolution under 10^{-8} Pa vacuum. The standard KBr disk method (1 mg of sample in 100 mg of KBr) was used. HRTEM observations were carried out on a JEM-2100 transmission electron microscope. X-ray photoelectron spectra (XPS) were recorded on a Thermo VG Escalab 250 X-ray photoelectron spectrometer at a pressure of ~2×10^{-9} Pa with $Al_{K\alpha}$ X-rays as the excitation source. The Cu K-edge XANES measurements were performed at beamline 1W1B of Beijing Synchrotron Radiation Facility (BSRF), Institute of High Energy Physics (IHEP), Chinese Academy of Sciences (CAS).

H_2-TPR and CO-TPD analyses were conducted in a quartz tube reactor on a Micromeritics ChemiSorb 2720 with a thermal conductivity detector (TCD). In a typical H_2-TPR process, 100 mg of a sample placed in a quartz tube reactor was first degassed under flowing argon at 400 °C for 2 h and cooled to RT. Then, a gaseous mixture of H_2 and Ar (1:9, v/v) was fed into the reactor at 40 mL min^{-1}. The temperature was raised to 700 °C at a heating rate of 10 °C min^{-1}. For the CO-TPD process, 100 mg of the reduced sample was first sealed and calcined in the reactor in the gaseous mixture of CO and Ar (1:9, v/v) at 400 °C for 1 h. Subsequently, the catalyst was purged in Ar at 500 °C for 30 min to remove excess CO, then cooled down to 25 °C for readsorption of CO; finally, the sample was subjected to a stream of Ar with a rate of 40 mL min^{-1} and a temperature ramp of 10 °C min^{-1} to perform the TPD. Furthermore, based on the difference of the CO chemisorption capacity over Ru/MgAl-LDH and Ru-Cu/MgAl-LDH (owing to the deposition of Cu on the surface of Ru particle), the Cu coverage (θ_{Cu}) was calculated by applying the following equation:

$$\theta_{Cu} = \frac{C_{Ru} - C_{Ru-Cu}}{C_{Ru}} \times 100 \quad (1)$$

in which C_{Ru} denotes the chemisorption capacity of CO per gram of the Ru/MgAl-LDH catalyst and C_{Ru-Cu} refers to the chemisorption capacity per gram of the Cu-decorated Ru catalyst.

In situ FTIR absorption spectroscopy of CO was performed in a quartz cell equipped with KBr windows allowing sample activation and successive measurements in the range 25–600 °C, at a pressures as low as 10^{-4} Pa. The samples (≈50 mg) were pressed into a disk and activated in the same cell for the measurement. FTIR spectra were collected with a Nicolet 380 instrument spectrophotometer with a resolution of 4 cm^{-1} and accumulation of 64 sans. After hydrogen treatment at 400 °C, the sample was cooled to 150 °C and scanned to get a background record below a pressure of 2×10^{-4} Pa. Then, the sample was exposed to a CO flow at 30 °C for another 120 min. Sample scanning for adsorbed CO was conducted after the pressure was again reduced below 2×10^{-4} Pa.

Computational methods

The Ru (0001), Ru (1122), and Cu cluster-decorated Ru (0001) facet were presented as a p(4×4) slab with a thickness of four Ru layers, only the bottom atoms in the slab were constrained to their crystal lattice positions. The neighboring slabs were separated in the direction perpendicular to the surface by a vacuum region of 15 Å.

First-principle calculations within the DFT framework were performed within the CASTEP code in the Materials Studio 6.1 software package.[51] The exchange-correlation potential was described by the Perdew–Burke–Ernzerhof (PBE) generalized gradient approach (GGA).[52] The structure optimizations are based on the following points: 1) an energy tolerance of 5.0×10^{-5} eV per atom; 2) a maximum force tolerance of 0.1 eV; 3) a maximum displacement tolerance of 5′10^{-3} Å. To study the interactions between Ru surface and cyclohexene, the adsorption energy is defined as E_{ads} and calculated based on the following equation:

$$E_{ads} = E(\text{Facet}) + E(\text{Cyclohexene}) - E(\text{Facet with Cyclohexene}) \quad (2)$$

Acknowledgements

This work was supported by the 973 Program (Grant No. 2011CBA00504), the National Natural Science Foundation of China (NSFC), the Scientific Fund from Beijing Municipal Commission of Education (20111001002) and the Fundamental Research Funds for the Central Universities (ZD 1303). We acknowledge the support of BSRF (Beijing Synchrotron Radiation Facility) during the XAFS measurements. M. W. particularly appreciates the finan-

cial aid from the China National Funds for Distinguished Young Scientists of the NSFC.

Keywords: benzene · cyclohexene · hydrogenation · layered double hydroxides · ruthenium

[1] a) H. Nagahara, M. Ono, M. Konishi, Y. Fukuoka, *Appl. Surf. Sci.* **1997**, *121*, 448 – 451; b) C. U. I. Odenbrand, S. T. Lundin, *J. Chem. Technol. Biotechnol.* **1981**, *31*, 660 – 669; c) M. Damm, B. Gutmann, C. O. Kappe, *ChemSusChem* **2013**, *6*, 978 – 982.

[2] a) G. Tavoularis, M. A. Keane, *Appl. Catal. A* **1999**, *182*, 309 – 316; b) E. Dietzsch, U. Rymsa, D. Hönicke, *Chem. Eng. Technol.* **1999**, *22*, 130 – 133.

[3] Y. Pei, G. B. Zhou, N. Luan, B. N. Zong, M. H. Qiao, F. Tao, *Chem. Soc. Rev.* **2012**, *41*, 8140 – 8162.

[4] P. Zhang, T. B. Wu, T. Jiang, W. T. Wang, H. Z. Liu, H. L. Fan, Z. F. Zhang, B. X. Han, *Green Chem.* **2013**, *15*, 152 – 159.

[5] J. L. Liu, Y. Zhu, J. Liu, Y. Pei, Z. H. Li, H. Li, H. X. Li, M. H. Qiao, K. N. Fan, *J. Catal.* **2009**, *268*, 100 – 105.

[6] H. J. Sun, H. X. Wang, H. B. Jiang, S. H. Li, S. C. Liu, Z. Y. Liu, X. M. Yuan, K. J. Yang, *Appl. Catal. A* **2013**, *450*, 160 – 168.

[7] W. Xue, Y. Song, Y. Wang, D. Wang, F. Li, *Catal. Commun.* **2009**, *11*, 29 – 33.

[8] H. J. Sun, Y. J. Pan, H. B. Jiang, S. H. Li, Y. X. Zhang, S. C. Liu, Z. Y. Liu, *Appl. Catal. A* **2013**, *464*, 1 – 9.

[9] a) G. B. Zhou, X. H. Tan, Y. Pei, K. N. Fan, M. H. Qiao, B. Sun, B. N. Zong, *ChemCatChem* **2013**, *5*, 2425 – 2435; b) Y. Zhao, J. Zhou, J. Zhang, S. Wang, *Catal. Commun.* **2008**, *9*, 459 – 464; c) W. T. Wang, H. Z. Liu, G. D. Ding, P. Zhang, T. B. Wu, T. Jiang, B. X. Han, *ChemCatChem* **2012**, *4*, 1836 – 1843.

[10] Y. Zhao, J. Zhou, J. Zhang, S. Wang, *Catal. Commun.* **2008**, *9*, 459 – 464.

[11] R. S. Suppino, R. Landers, A. J. G. Cobo, *Appl. Catal. A* **2013**, *452*, 9 – 16.

[12] G. Zhou, Y. Pei, Z. Jiang, K. Fan, M. Qiao, B. Sun, B. Zong, *J. Catal.* **2014**, *311*, 393 – 403.

[13] F. Schwab, M. Lucas, P. Claus, *Green Chem.* **2013**, *15*, 646 – 649.

[14] F. Schwab, M. Lucas, P. Claus, *Angew. Chem. Int. Ed.* **2011**, *50*, 10453 – 10456; *Angew. Chem.* **2011**, *123*, 10637 – 10640.

[15] J. Struijk, M. d'Angremond, W. J. M. Lucas-de Regt, J. J. F. Scholten, *Appl. Catal. A* **1992**, *83*, 263 – 295.

[16] J. Q. Wang, P. J. Guo, S. R. Yan, M. H. Qiao, H. X. Li, K. N. Fan, *J. Mol. Catal. A* **2004**, *222*, 229 – 234.

[17] H. Z. Liu, S. G. Liang, W. T. Wang, T. Jiang, B. X. Han, *J. Mol. Catal. A* **2011**, *341*, 35 – 41.

[18] H. Z. Liu, T. Jiang, B. X. Han, S. G. Liang, W. T. Wang, T. B. Wu, G. Y. Yang, *Green Chem.* **2011**, *13*, 1106 – 1109.

[19] a) C. Fan, Y. A. Zhu, X. G. Zhou, Z. P. Liu, *Catal. Today* **2011**, *160*, 234 – 241; b) J. Bu, J. Q. Wang, M. H. Qiao, S. R. Yan, H. X. Li, K. N. Fan, *Acta Chim. Sin.* **2007**, *65*, 1338 – 1342; c) J. Bu, J. L. Liu, X. Y. Chen, J. H. Zhuang, S. R. Yan, M. H. Qiao, H. Y. He, K. N. Fan, *Catal. Commun.* **2008**, *9*, 2612 – 2615.

[20] J. Liu, S. He, C. Li, F. Wang, M. Wei, D. G. Evans, X. Duan, *J. Mater. Chem. A* **2014**, *2*, 7570 – 7577.

[21] a) K. M. Bratlie, H. Lee, K. Komvopoulos, P. Yang, G. A. Somorjai, *Nano Lett.* **2007**, *7*, 3097 – 3101; b) G. F. Liang, L. M. He, M. Arai, F. Y. Zhao, *ChemSusChem* **2014**, *7*, 1415 – 1421.

[22] a) J. H. Kwak, L. Kovarik, J. Szanyi, *ACS Catal.* **2013**, *3*, 2449 – 2455; b) J. H. Kwak, L. Kovarik, J. Szanyi, *ACS Catal.* **2013**, *3*, 2094 – 2100.

[23] S. C. Tsang, N. Cailuo, W. Oduro, A. T. S. Kong, L. Clifton, K. M. K. Yu, B. Thiebaut, J. Cookson, P. Bishop, *ACS Nano* **2008**, *2*, 2547 – 2553.

[24] N. Kumar, T. S. King, R. D. Vigil, *Chem. Eng. Sci.* **2000**, *55*, 4973 – 4979.

[25] J. A. Gursky, S. D. Blough, C. Luna, C. Gomez, A. N. Luevano, E. A. Gardner, *J. Am. Chem. Soc.* **2006**, *128*, 8376 – 8377.

[26] a) F. Z. Zhang, X. F. Zhao, C. H. Feng, B. Li, T. Chen, W. Lu, X. D. Lei, S. L. Xu, *ACS Catal.* **2011**, *1*, 232 – 237; b) Y. F. He, J. T. Feng, Y. Y. Du, D. Q. Li, *ACS Catal.* **2012**, *2*, 1703 – 1710; c) X. Zhang, Z. Wang, N. L. Qiao, S. Q. Qu, Z. P. Hao, *ACS Catal.* **2014**, *4*, 1500 – 1510.

[27] a) G. R. Williams, D. O'Hare, *J. Mater. Chem.* **2006**, *16*, 3065 – 3074; b) A. M. Fogg, A. L. Rohl, G. M. Parkinson, D. O'Hare, *Chem. Mater.* **1999**, *11*, 1194 – 1200.

[28] H. C. Liu, E. Z. Min, *Green Chem.* **2006**, *8*, 657 – 662.

[29] a) J. D. Hong, W. Zhang, Y. B. Wang, T. H. Zhou, R. Xu, *ChemCatChem* **2014**, *6*, 2315 – 2321; b) K. H. Goh, T. T. Lim, Z. L. Dong, *Water Res.* **2008**, *42*, 1343 – 1368; c) C. M. Li, Y. D. Chen, S. T. Zhang, J. Y. Zhou, F. Wang, S. He, M. Wei, D. G. Evans, X. Duan, *ChemCatChem* **2014**, *6*, 824 – 831; d) J. H. Lee, H. Kim, Y. S. Lee, D. Y. Jung, *ChemCatChem* **2014**, *6*, 113 – 118.

[30] S. He, C. M. Li, H. Chen, D. S. Su, B. S. Zhang, X. Z. Cao, B. Y. Wang, M. Wei, D. G. Evans, X. Duan, *Chem. Mater.* **2013**, *25*, 1040 – 1046.

[31] C. M. Li, Y. D. Chen, S. T. Zhang, S. M. Xu, J. Y. Zhou, F. Wang, M. Wei, D. G. Evans, X. Duan, *Chem. Mater.* **2013**, *25*, 3888 – 3896.

[32] C. M. Li, J. Y. Zhou, W. Gao, J. W. Zhao, J. Liu, Y. F. Zhao, M. Wei, D. G. Evans, X. Duan, *J. Mater. Chem. A* **2013**, *1*, 5370 – 5376.

[33] C. Li, L. Y. Wang, M. Wei, D. G. Evans, X. Duan, *J. Mater. Chem.* **2008**, *18*, 2666 – 2672.

[34] M. Q. Zhao, Q. Zhang, J. Q. Huang, F. Wei, *Adv. Funct. Mater.* **2012**, *22*, 675 – 694.

[35] J. B. Han, J. Lu, M. Wei, Z. L. Wang, X. Duan, *Chem. Commun.* **2008**, 5188 – 5190.

[36] A. E. Palomares, J. G. Prato, F. Rey, A. Corma, *J. Catal.* **2004**, *221*, 62 – 66.

[37] J. T. Kloprogge, R. L. Frost, *J. Solid State Chem.* **1999**, *146*, 506 – 515.

[38] a) J. Álvarez-Rodríguez, B. Bachiller-Baeza, A. Guerrero-Ruiz, I. Rodríguez-Ramos, A. Arcoya-Martín, *Catal. Today* **2008**, *133*, 793 – 799; b) J. Álvarez-Rodríguez, B. Bachiller-Baeza, A. Guerrero-Ruiz, I. Rodríguez-Ramos, A. Arcoya-Martín, *Microporous Mesoporous Mater.* **2006**, *97*, 122 – 131.

[39] E. Asedegbega-Nieto, B. Bachiller-Baeza, A. Guerrero-Ruiz, I. Rodríguez-Ramos, *Appl. Catal. A* **2006**, *300*, 120 – 129.

[40] R. Kötz, H. J. Lewrenz, S. Stucki, *J. Electrochem. Soc.* **1983**, *130*, 825 – 829.

[41] J. Hedman, M. Klasson, R. Nilsson, C. Nordling, M. F. Sorokina, O. I. Kljushnikov, S. A. Nemnonov, V. A. Trapeznikov, V. G. Zyranov, *Phys. Scr.* **1971**, *4*, 195 – 201.

[42] J. B. Han, Y. B. Dou, J. W. Zhao, M. Wei, D. G. Evans, X. Duan, *Small* **2013**, *9*, 98 – 106.

[43] E. V. Ramos-Fernández, J. Silvestre-Albero, A. Sepúlveda-Escribano, F. Rodríguez-Reinoso, *Appl. Catal. A* **2010**, *374*, 221 – 227.

[44] S. X. Xia, R. F. Nie, X. Y. Lu, L. N. Wang, P. Chen, Z. Y. Hou, *J. Catal.* **2012**, *296*, 1 – 11.

[45] X. W. Chen, J. J. Delgado, J. M. Gatica, S. Zrrad, J. M. Cies, S. Bernal, *J. Catal.* **2013**, *299*, 272 – 283.

[46] M. W. Smale, T. S. King, *J. Catal.* **1989**, *119*, 441 – 450.

[47] a) R. T. Vang, K. Honkala, S. Dahl, E. K. Vestergaard, J. Schnadt, E. Laegsgaard, B. S. Clausen, J. K. Nørskov, F. Besenbacher, *Nat. Mater.* **2005**, *4*, 160 – 162; b) L. D. Shao, X. Huang, D. Tescher, W. Zhang, *ACS Catal.* **2014**, *4*, 2369 – 2373.

[48] S. C. Liu, Y. Q. Guo, X. L. Yang, Y. L. Ji, G. Luo, *Chin. J. Catal.* **2003**, *24*, 42 – 46.

[49] D. W. Goodman, C. H. F. Peden, *J. Catal.* **1985**, *95*, 321 – 324.

[50] Z. J. Wu, Y. Z. Mao, X. X. Wang, M. H. Wang, *Green Chem.* **2011**, *13*, 1311 – 1316.

[51] a) B. Delley, *J. Chem. Phys.* **1990**, *92*, 508 – 517; b) B. Delley, *J. Chem. Phys.* **1996**, *100*, 6107 – 6110.

[52] a) J. P. Perdew, J. A. Chevary, S. H. Vosko, K. A. Jackson, M. R. Perderson, D. J. Singh, C. Fiolhais, *Phys. Rev. B* **1992**, *46*, 6671 – 6687; b) J. P. Perdew, J. A. Chevary, S. H. Vosko, K. A. Jackson, M. R. Perderson, D. J. Singh, C. Fiolhais, *Phys. Rev. B* **1993**, *48*, 4978 – 4978; c) J. P. Perdew, K. Burke, Y. Wang, *Phys. Rev. B* **1996**, *54*, 16533 – 16539; d) J. P. Perdew, K. Burke, Y. Wang, *Phys. Rev. B* **1998**, *57*, 14999 – 14999.

Received: November 4, 2014
Revised: December 23, 2014
Published online on January 28, 2015